Journal Name

ARTICLE

A fluorescent molecular rotor showing vapochromism, aggregation-induced emission, and environmental sensing in living cells

Received 00th January 20xx,
Accepted 00th January 20xx

DOI: 10.1039/x0xx00000x

www.rsc.org/

Matthias Koenig,[d] Barbara Storti,[e] Ranieri Bizzarri,[e] Dirk M. Guldi,[d] Giuseppe Brancato*[c] and Giovanni Bottari*[ab]

Among the plethora of recently proposed molecular sensors, those belonging to the class of fluorescent molecular rotors (FMRs) have attracted much attention owing to their peculiar photophysical properties that enable an unprecedented sensitivity towards environmental microviscosity. The usual FMR synthetic design prescribes chromophores characterized by an intramolecular rotation between two well-defined excited states, a locally excited state and a twisted internal charge transfer (TICT) state, where the sensing capabilities arise from a dual competition of the corresponding radiative/non-radiative decay processes. However, we have recently demonstrated a different modus operandi of a new subclass of solvatochromic FMRs, which exploit a solvent-independent, barrier-free intramolecular rotation of the excited dye. The rotational dynamics is modulated by local viscosity and, in turn, manifested through a variable spectral signal. In order to translate the same rotational mechanism in a versatile sensor of polarity and viscosity, we designed and thoroughly characterized a novel FMR, namely 4-(triphenylamino)-phthalonitrile (**TPAP**). Remarkably, in addition to a high sensitivity versus solvent polarity and viscosity, **TPAP** is also able to form stable fluorescent nanoparticles characterized by aggregation-induced emission, via a simple sonochemical treatment. Such peculiar features are tested in different applications aiming at illustrating its capability to report on solvatochromic and vapochromic effects, as well as to provide detailed intracellular information through bioimaging studies.

Introduction

Fluorophores whose emission changes in response to variations in their environment have emerged as an interesting family of compounds with widespread applications in analytical, environmental, optical, and biochemical areas. In this context, sensors for polarity and viscosity are the most expedient ones, owing to their widespread applicability in several life-science studies.[1] The polarity sensitivity is generally based on the change in dipole moment of the fluorophore upon photo-excitation and the resulting dipolar relaxation of the surrounding molecules or residues. This effect is called solvatochromism and is accounted for by several theoretical descriptions, among which stands the Lippert-Mataga model[2] for its simplicity and effective interpretation of many experimental data.[3-5]

Fluorophores sensitive to local viscosity are referred to as *fluorescent molecular rotors* (FMR).[6] FMRs perceive local viscosity through intramolecular twisting motion(s) that occur at excited state.[7] In most cases, intramolecular distortion leads to a twisted internal charge transfer (TICT) state, which is almost non-emissive. Thus, slowing the twisting motions as viscosity increases leads to stronger emission and longer lifetime decay.[8] The Forster-Hoffmann model of molecular rotors[9] affords a reliable quantitative description of fluorescence dependence on viscosity for most FMRs.[10] Nonetheless, a common drawback of FMRs is the difficulty to predict their sensitivity towards local polarity, owing to the complex dipolar properties of accessible excited states.[11] Some FMRs are even insensitive to the dielectric properties of their surrounding environment.[12] In this context, probes reporting predictably on both polarity and viscosity are a desirable tool in the field of fluorescence molecular sensors, since they may allow for a thorough physicochemical characterization of their local environment.

We recently described a prototype for a new class of molecular rotors, namely 4-(diphenylamino)-phthalonitrile (**DPAP**), which combines strong fluorochromism and viscosity response within one molecule.[13] This unique feature is attributed to an unprecedented and distinctive *modus operandi,* which is based on an unusual barrier-less and solvent-independent flexibility that finely modulates its photophysical properties. Motivated by these

[a] Departamento de Química Orgánica, Universidad Autónoma de Madrid, 28049, Cantoblanco, Spain. E-mail: giovanni.bottari@uam.es
[b] IMDEA-Nanociencia, Campus de Cantoblanco, C/Faraday 9, 28049 Madrid, Spain
[c] Scuola Normale Superiore, Piazza dei Cavalieri 7, I-56126 Pisa, Italy. E-mail: giuseppe.brancato@sns.it
[d] Department of Chemistry and Pharmacy & Interdisciplinary Center for Molecular Materials (ICMM), Friedrich-Alexander-Universität Erlangen-Nürnberg, 91058, Erlangen, Germany
[e] NEST, Istituto Nanoscienze-CNR and Scuola Normale Superiore, Piazza San Silvestro 12, I-56127 Pisa, Italy

† Footnotes relating to the title and/or authors should appear here.
Electronic Supplementary Information (ESI) available: Additional photophysical studies, computational details. See DOI: 10.1039/x0xx00000x

findings, we here present 4-(triphenylamino)-phthalonitrile (**TPAP**, Fig. 1a), a FMR designed to exploit the same atypical mechanism with an increased charge transfer distance. **TPAP** is easily synthesized in a few steps via a simple and convergent route and makes use of an amino electron donor unit and two nitrile electron acceptor units to facilitate intramolecular charge transfer (ICT) upon photoexcitation. The extended π-conjugated system of **TPAP** is designed to facilitate the formation of a charge transfer state, which, in turn, does affect its electronic and spectroscopic features, as well as its sensitivity towards the environment. In this work, we embarked on a thorough photophysical and computational study to analyze **TPAP** solvatochromism and viscosity response. On this account, **TPAP** has been tested in three different applications requiring environmental sensing. Our goal was to assess the feasibility and *modus operandi* of **TPAP** in different contexts, including its capability to report fluorescence emission and lifetime differences in the cellular environment.

First, **TPAP** was shown to exhibit excellent vapochromic response when exposed to a range of different solvent vapors. Hence, **TPAP** was demonstrated to give rise to the formation of highly-fluorescent organic nanoparticles based on an aggregation-induced emission (AIE) mechanism.[14] Finally, **TPAP** was investigated as a dual polarity and viscosity probe in living cells, on account of the fundamental relevance of electrostatic interactions[15-17] and diffusion-controlled reactions to sustain life.[6] The sensing capability of **TPAP** is exploited by a new imaging approach, named *phasor analysis*, which relies on a simple graphic analysis of spectral and lifetime fluorescence images following a mathematical transformation.[18] Overall, our results do support the use of **TPAP** as an outstanding probe in the field of environmental sensors.

Materials and methods

Synthesis of TPAP

TPAP was prepared and purified following the reported procedure.[19] **TPAP** was characterized by ^{1}H and ^{13}C NMR, elemental analysis, mass spectrometry and IR, and the data obtained, that can be found in the Supporting Information, matched with the values reported in the literature.

Preparation of TPAP AIE dispersions

For the preparation of the **TPAP** dispersions in a 87/13 water/methanol mixture, a solution of **TPAP** in methanol (286 µL) was added to deionized water (1914 µL) under vigorous stirring (final volume of the prepared solvents mixture = 2200 µL). A similar procedure, but using different ratio of the solution of **TPAP** in methanol and deionized water, has been used for the preparation of the other mixtures which present different water/methanol ratio. The water/methanol mixtures at different **TPAP** concentration (from 1.1×10^{-6} up to 5.0×10^{-4} M) were obtained using methanol solutions at different **TPAP** concentration.

Preparation of TPAP films for vapochromic studies

TPAP films for vapochromic studies were prepared by uniformly spreading a hexane solution of **TPAP** on a glass slide and letting the solvent to evaporate. Residual traces of the solvent were eliminated by introducing the **TPAP**-coated glass slides in a vacuum chamber. The vapochromic studies were carried out by placing these coated slides into a chamber saturated with the vapours of different solvents while illuminating the slides with a 365 nm lamp.

Cell cultures

CHO cells were grown in Dulbecco's modified Eagle medium: F-12 nutrient mix (D-MEM/F-12) purchased from Invitrogen (Carlsbad, CA) supplemented with 10% fetal bovine serum and 100 U/ml penicillin, and 100 mg/ml streptomycin (Invitrogen). Cells were maintained at 37 °C in a humidified 5% CO_2 atmosphere. For fluorescence imaging, 120000 cells were plated onto a 35-mm glass-bottom dish (WillCo-dish GWSt-3522).

More details on quantum mechanical (QM) calculations, fluorescence microscopy imaging of living cells, photophysical studies of **TPAP** in solution and dispersions, cryogenic transmission electron microscopy (Cryo−TEM) studies and dynamic light scattering (DLS) measurements can be found in the Supporting Information section.

Results and discussion

TPAP structural analysis

The peculiar chemical structure of **TPAP** confers significant rotational freedom to its phenyl rings, while the backbone of the molecule is constrained to a Y-shaped configuration. From the computed optimized structure, it has been observed that the nitrogen atom is coplanar with its covalently linked carbon atoms, according to a sp^2 hybridization. Due to steric hindrance, the amine phenyl groups assume a propeller-like configuration, as shown in Fig. 1b, and their rotational motion is therefore concerted. On the other hand, the 1,2-dicyanobenzene moiety can rotate rather freely with respect to the rest of the molecule (see Fig. S1), showing relatively small energetic barriers (<3 kcal/mol) along the computed torsional potential.

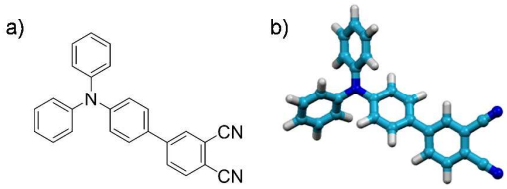

Fig. 1: a) Molecular and b) optimized structure of **TPAP**.

TPAP optical properties and solvatochromism

Optical absorption and emission spectra of **TPAP** were recorded in various solvents and solvent mixtures of different polarity (Table S1). The absorption spectra of **TPAP** in cyclohexane, *o*-xylene, THF and acetonitrile are shown in Fig. 2a. All spectra are characterized by two broad bands with maxima at about 390 nm and 285 nm. QM calculations have assigned these bands to transitions from S0 to S1 and S4, respectively (see Fig. S2 for the computed optical spectra).

Extinction coefficients of about 2 × 10^4 M^{-1} cm^{-1} were observed in all solvents. However, a strong increase in absorption with extinction coefficients rising to 1 × 10^5 M^{-1} cm^{-1} was noted in pyridine (Fig. S3). This finding may suggest that π–π interactions with the solvent are responsible for the observed absorption enhancement.

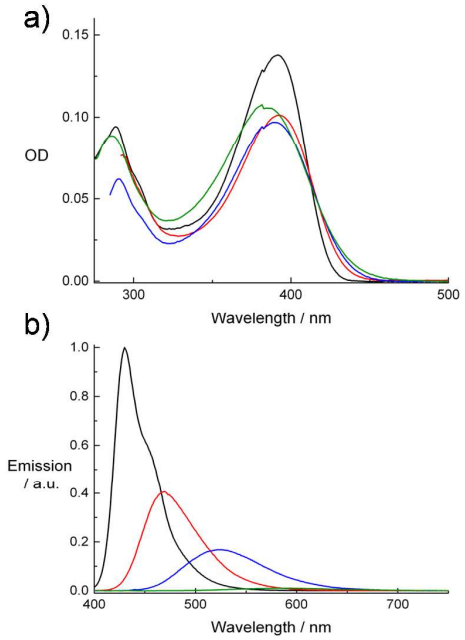

Fig. 2: a) Absorption and b) emission spectra (λ_{exc} = 392 nm) of **TPAP** ([**TPAP**] = 5 × 10^{-6} M and 1 × 10^{-6} M in a) and b), respectively) in cyclohexane (black), *o*-xylene (red), THF (blue) and acetonitrile (green).

Emission spectra recorded in cyclohexane, *o*-xylene, THF and acetonitrile are shown in Fig. 2b upon excitation at the absorption maximum (392 nm). In contrast to absorption, a strong solvatochromic effect is observed in the recorded emission spectra, affecting both emission energies and intensities. It is worth noting that a single, broad emission signal evolves in all solvents except for cyclohexane for which an additional small shoulder was detected. In this case, QM calculations have confirmed the nature of the emission as occurring from a relaxed S1 state and have nicely matched the observed solvatochromism in going from apolar to polar solvents (see Fig. S2).

For a detailed description of **TPAP** solvatochromism, the Lippert-Mataga polarity parameter (Δf) was evaluated for an extended set of solvents and solvent mixtures according to eq S1 (Table S1).[20,21] Fig. 3a shows the correlations between the optical absorption and emission maxima and Δf.

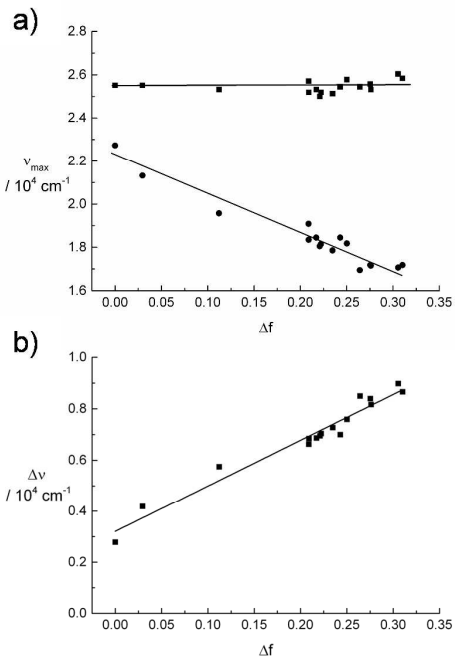

Fig. 3: a) Plot of the absorption (squares) and emission (circles) maxima of **TPAP** as a function of the solvent polarity parameter (Δf). b) Lippert plot of **TPAP** as a function of Δf.

As previously shown for a few solvents, polarity has a little effect on the absorption maximum of **TPAP**, while the emission is associated with a significant solvatochromic effect. Remarkably, in strongly polar solvents, a Stokes shift as large as 200 nm is observed. The good linear correlation with Δf furthermore suggests that the nature of the fluorescent state is virtually equivalent in all applied solvents.

Next, to estimate the polarity sensitivity of **TPAP**, a Lippert plot was created by plotting the Stokes' shift against Δf according to the Lippert-Mataga equation (eq. 1), resulting in a linear correlation (Fig. 3b). Here, Δμ describes the change in dipole moment upon excitation and can be used as a measure for solvent sensitivity of the fluorophore.[21] From the slope of the Lippert Plot, we could estimate a Δμ value of 17.4 D for **TPAP** (Note that computed Δμ for **TPAP** are 17.7 D and 12.7 D in acetonitrile and hexane, respectively). This significant dipole change is attributed to the strong ICT character of the excited state, owing to the extended π-system that enables a better charge separation between the oxidation and reduction centers of the molecule, and thereby increasing Δμ in a significant way.

$$\Delta\nu = \Delta\nu_0 + \frac{2(\mu_e - \mu_g)^2}{hcr^3}\Delta f \quad \text{(eq. 1)}$$

Fluorescence quantum yields (Φ) and emission lifetimes (τ) of **TPAP** were determined in several solvents and are listed in Table S1. Φ values of **TPAP** are generally very high in apolar solvents, while they are low (< 0.2) in polar and protic milieu (Fig. S4). The Φ linearly decreases with increasing solvent

polarity and, in turn, it confirms the trend established in the emission and Lippert plots.

All emission time decays were fitted by a mono-exponential function. Interestingly, τ values were found to increase linearly up to Δf = 0.22 – 0.25, while in the high polarity region a sudden decrease set in (Fig. S5). This odd behaviour prompted us to separate out the radiative (k_r) from the non-radiative (k_{nr}) decay rate constants by eq. S2 (Table S1). k_r values showed good linearity when plotted versus Δf (Fig. 4a). In contrast, k_{nr} *vs.* Δf was associated with a different trend (Fig. 4b). For solvents with Δf < 0.22–0.25, the polarity of the medium had no influence on k_{nr}. However, in the high-polar solvent region (Δf > 0.22–0.25) a sudden increase in k_{nr} was detected. This effect was extremely pronounced in protic polar solvents such as methanol and ethylene glycol, suggesting a possible hydrogen-bonding stabilization of the ICT state.

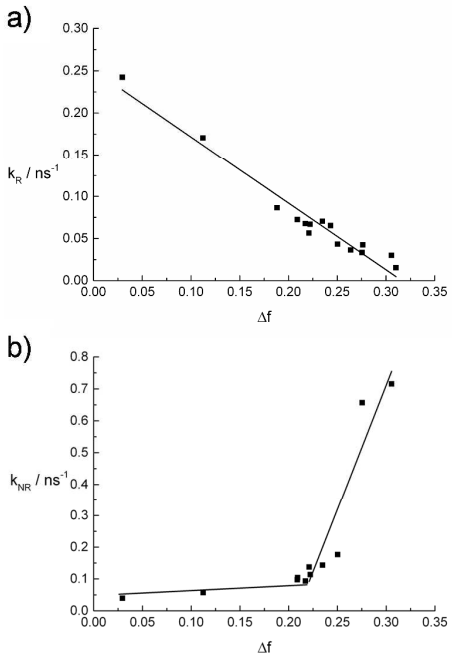

Fig. 4: Plot of the solvent parameter Δf versus a) the fluorescence radiative decay rate constant (k_R) and b) estimated non-radiative decay rate constant (k_{NR}) for **TPAP**.

Interestingly, beside the above mentioned solvatochromic response, **TPAP** also exhibit a strong vapochromic response. The emission wavelength of **TPAP** films (λ_{exc} = 365 nm) strongly varied when exposed to vapors of solvents with different polarity as observed by naked eye (Fig. 5). In all cases, solvent vapors could be reversibly adsorbed by and removed from the films, with no apparent loss of emission efficiency. These results support the use of **TPAP** and structurally-related compounds[22] as a new chromogenic material suitable for the detection of volatile organic compounds (VOCs). Notably, the recent application of the hue parameter of the HSV color-space for spectral fluorescent sensing[23] could open the way to a cost-effective way to identify vapours and vapour mixtures by means inexpensive RGB cameras.

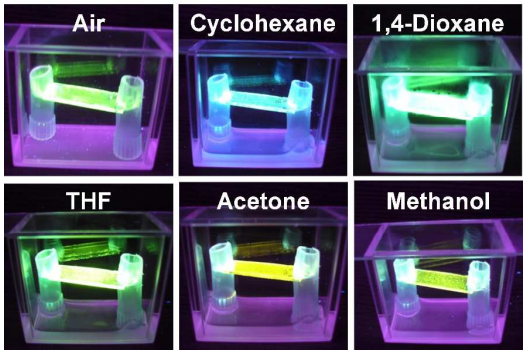

Fig. 5: Vapochromism of **TPAP** films on glass exposed to air and vapors of different solvents. Excitation wavelength for all samples was 365 nm.

Characterization of TPAP triplet state

Nanosecond transient absorption experiments with excitation at 355 nm were carried out in oxygen-free THF solutions to characterize the triplet state of **TPAP**. The triplet state of **TPAP** showed a maximum at 700 nm that decayed over several μs (Fig. S7). Quenching experiments with molecular oxygen confirmed the triplet nature of the detected absorption, with a quenching constant of 6.5 × 10^8 $M^{-1}s^{-1}$. Fitting the transient absorption decay traces resulted in a triplet lifetime of 26 μs for **TPAP** in THF (Figure S7, inset).

In this context, singlet oxygen quantum yields, gathered at 1275 nm for **TPAP** in different solvents, helped us to confirm the solvent dependency of the triplet state formation (Fig. S8).[24,25] The largest production of singlet oxygen was detected in *o*-xylene (Φ_Δ = 0.16), the less polar solvent, followed by THF (Φ_Δ = 0.13). Notably, comparison of these figures with the Φ in the same apolar solvents indicated that intersystem crossing to triplet accounts for a large fraction of the non-radiative depopulation of the singlet excited state. Conversely, in polar solvents like acetonitrile almost no singlet oxygen could be detected (Φ_Δ = 0.01). The low Φ of **TPAP** in polar solvents suggested that non-radiative decay channels connecting singlet excited and ground states become largely predominant.

Transient absorption measurements on TPAP solutions

To shed light on the excited state processes and the deactivation pathways of **TPAP**, femtosecond transient absorption spectroscopy was carried out in different solvents (*o*-xylene, THF, acetonitrile and methanol). Photoexcitation (pump) was set at 387 nm, and transient spectra were collected at different times in the 400–1100 nm range (Fig. 6). In all solvents, a large positive absorption appeared at 450–500 nm; smaller positive bands were detected between 550–1100 nm (Fig. 6a). Notably, the band in the 500–600 nm region was found to change in < 10 ps, witnessing the dipolar relaxation of the surrounding solvent molecules (*i.e.*, 1-10 ps is the characteristic time of apolar solvent rearrangement around solvatochromic dyes).[26]

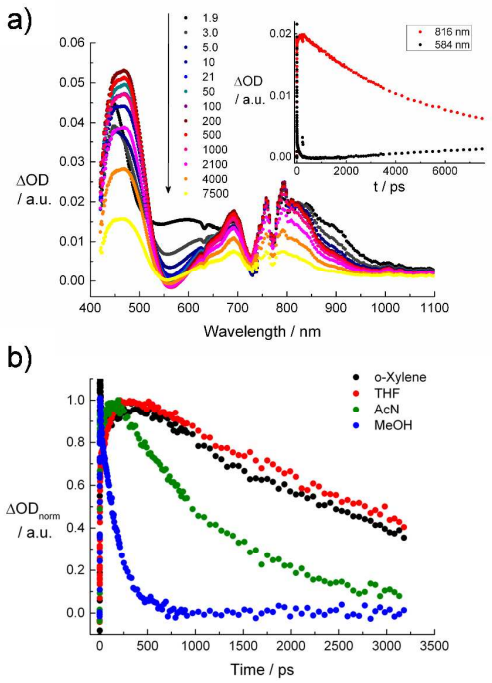

Fig. 6: a) Differential absorption spectra of **TPAP** obtained upon femtosecond flash photolysis in argon-saturated THF with several time delays between 0 and 7500 ps (see legend for details). OD at the 387 nm excitation wavelength was 0.2 – 0.3. Inset: time–absorption profiles in THF monitoring intersystem crossing with singlet decay (red) and triplet formation (black). b) Time–absorption profiles in *o*-xylene (black), THF (red), acetonitrile (green) and methanol (blue) monitored at 480 nm.

Owing to its intensity, the high-energy absorption at 450–500 nm was followed over time from 1 to 3500 ps. Time-plots of absorption at 480 nm showed faster kinetics in polar and protic solvents (acetonitrile and methanol) as compared to medium-polarity or apolar milieu (Fig. 6b). In all cases, the transient profile decayed almost biexponentially (Table S2). The faster component (rate constant k_1) referred to a 10–100 ps kinetic process. The slower component (rate constant k_2) was attributed to the return to the ground state and was characterized by a time constant similar to fluorescence lifetime values. Plot of k_1 and k_2 *vs.* the solvent polarity parameter Δf resembled the relationship established for the non-radiative decay constants k_{NR} – *vide supra* (Fig. S6). These findings highlight the strong influence of solvent polarity in determining ICT formation and depopulation.

Viscosity dependence of TPAP fluorescence

Along with a strong solvatochromism, **TPAP** also presents a good response to the solvent viscosity (η), especially in polar and protic solvents where non-radiative deactivation of excited state is predominant (*vide supra*). Increasing the solvent viscosity should lead to a decrease in the rotor's flexibility with a smaller interval and lower total values of the average dihedral angle being accessible. This influences the rotor's deactivation pathways by shifting towards a more radiative decay.[27]

Experimentally, we measured fluorescence emission, in media characterized by high and constant polarity values and variable viscosities. Fig. 7 shows the emission changes for **TPAP** in protic solvents such as methanol (η = 0.52 at 298 K), ethylene glycol (η = 16.2 at 298 K), and glycerine (η = 950 at 298 K). Upon increasing the solvent viscosity, we observed a clear increase of emission intensity accompanied by a significant blue-shift. It is worth noting that shift of the emission wavelength upon changing viscosity is generally not observed for TICT rotors, where emission emerges from an energetically invariable locally-excited state.[10]

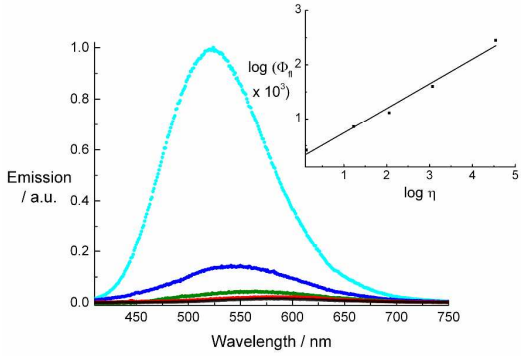

Fig. 7: Emission of **TPAP** in solvents of different viscosity: Methanol (black), ethylene glycol (red), ethylene glycol/glycerine (1:1) (green), glycerine at 295 K (blue), and glycerine at 265 K (cyan) The optical density at the 395 nm excitation wavelength was 0.09 for all samples. Inset: Double-logarithmic plot of the solvent viscosity (η) versus the fluorescent quantum yield (Φ_{fl}) for **TPAP** according to the Förster-Hoffmann equation.

Next, we investigated further the system plotting η *vs.* Φ_{fl} for five solvents/solvent mixtures. Data complied with the Förster-Hoffmann equation (eq. 2) (Fig. 7, inset),[28] which predicts linearity on a double logarithmic scale on account of the response of conformational motions to the solvent viscosity. **TPAP** shows high sensitivity towards viscosity changes as witnessed by the Förster-Hoffmann slope x = 0.46. Notably, this value is in keeping with the figures determined for most fluorescent rotors.[29]

$$\log \Phi_{fl} = x \log \eta + C \quad \text{(eq. 2)}$$

As high solvent polarity mainly affects the non-radiative decay pattern, transient absorption spectroscopy experiments were additionally carried out by inspecting the absorption band located at 480 nm. Upon increasing the viscosity from methanol to glycerol, lifetimes increased significantly by a factor of 10 for the short-lived compound k_1 (formation) and by a factor of 4 for the longer-lived compound k_2 (decay) (Table S2). Similarly, a double-logarithmic plot according to the modified Förster-Hoffmann equation was created and revealed linear dependency in the investigated viscosity interval for both k_1 and k_2 (Fig. S9).

Aggregation-induced emission studies on TPAP

To evaluate the dependence of **TPAP** emission upon aggregation, we investigated **TPAP** nanoparticles formed in aqueous media by the reprecipitation method.[30]

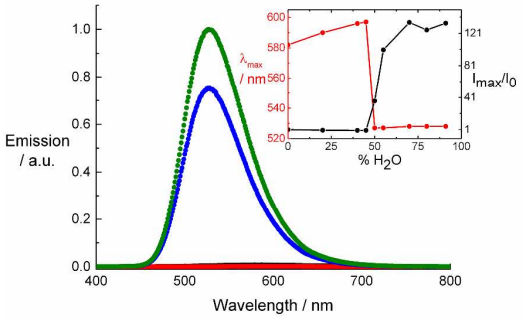

Fig. 8: Fluorescence emission (λ_{exc} = 390 nm) of **TPAP** ([**TPAP**] = 4.5 x 10^{-5} M) in methanol (black) and in 45/55 (v/v) (red), 55/45 (v/v) (blue) and 87/13 (v/v) (green) water/methanol mixtures. Inset: Relative emission intensity (right) and emission maximum wavelength (left) of water/methanol mixtures of **TPAP** as a function of the water content.

Notably, the fluorescence of **TPAP** was found to quench upon addition of a small amount of water to a methanol solution. This effect was attributed to the increase in solvent polarity that favoured non-radiative deactivation. However, when the water content exceeded 50% (v/v), the emission gradually intensified reaching a maximum for a water content of around 70% (Fig. 8, inset). The astounding emission increase (120-fold) was attributed to **TPAP** aggregation and it largely surpasses the emission enhancement obtained with **DPAP** (20-fold emission increase).[31] At the same time, a blue-shift of the emission maximum of *ca.* 70 nm (from 600 to 528 nm) and a red shift of the absorption maximum from 390 (methanol) to 414 nm (87/13 (v/v) water/methanol mixture) was noticed. Absorption spectra were accompanied by a broad tail reaching to almost 800 nm, which give further evidence to the formation of **TPAP** aggregates (Fig. S10). In addition, upon freezing the **TPAP** water/methanol mixture, a further emission increase (ca. 1.3-fold) was observed (Fig. 9).[32,33]

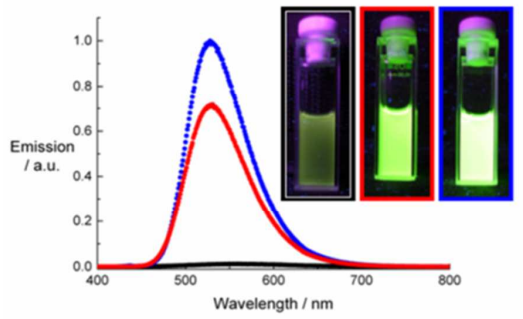

Fig. 9: Fluorescence emission (λ_{exc} = 390 nm) of **TPAP** (4.5 × 10^{-5} M) in methanol (black) and 87/13 (v/v) water/methanol mixtures at room temperature (red) and frozen (green). **TPAP** concentration in both solution and dispersions is 4.5 × 10^{-5} M. Inset: Pictures of the three cuvettes used for the fluorescent experiments upon illumination at 365 nm. The coloured boxes around each picture follow the same colour-code used for the fluorescence experiments.

Lifetime studies helped to better rationalize the observed photophysical behaviour. As compared to methanol solution (τ = 0.17 ns), fluorescence lifetime increased up to 12.9 ns for the AIE dispersions and even further (14.3 ns) upon freezing the **TPAP** dispersion (Fig. S13, Table S3). The lifetime increase was consistent with the increase in their emission intensities (*vide supra*). The emission for **TPAP** nanoparticle dispersions decays biexponentially. Time-resolved emission spectroscopy (TRES) highlighted a clear blue-shift of about 20 nm in the 0.5–20 ns time range. This finding suggested the presence of a faster component emitting at shorter wavelengths and a slower component emitting at longer wavelengths (Fig. S14). Indeed, an analysis of the deconvoluted, time-resolved emission spectra corroborated this concept (Fig. S15). From these observations and literature data,[34,35] we speculated that in the **TPAP** aggregates the local charge-transfer within a monomer is accompanied by intermolecular delocalization of the charge-separated state which deactivates via a long-lived and red-shifted emission.

Dispersions at different **TPAP** concentrations were prepared in an 87/13 (v/v) water/methanol mixture.[36] These studies showed that AIE set in above 1 μM **TPAP** (Fig. S11), which is much lower compared to the figure relevant to **DPAP** (20 μM). **TPAP** dispersions were found to be reasonably stable for a few hours; also, ultrasonication did not prompt changes in structure, emission and stability.

The structural properties of **TPAP** aggregates were studied by dynamic light scattering (DLS) and cryogenic-transmission electron microscopy (cryo-TEM) techniques. DLS showed that the **TPAP** aggregates correspond to nanoparticles with radius below 300 nm. The nanoparticle size decreased upon increasing the water content of the dispersing medium (Fig. 10). On the other hand, **TPAP** concentration did not affect the nanoparticle radius (Fig. S12).

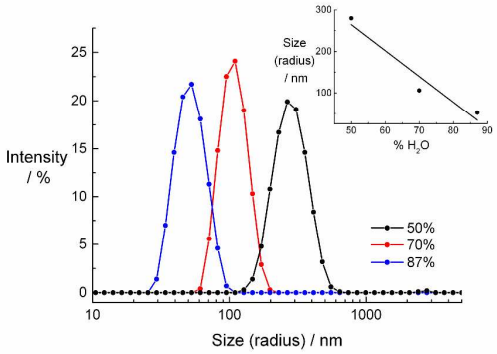

Fig. 10: Dynamic light scattering (DLS) measurements of **TPAP** dispersions ([**TPAP**] = 4.5 × 10^{-5} M) in different water/methanol mixtures (50/50 (v/v) (black), 70/30 (v/v) (red) and 87/13 (v/v) (blue)). Inset: Plot of the average hydrodynamic radius *vs*. the water content.

Consistently with DLS results, cryo-TEM on a 87/13 (v/v) water/methanol highlighted both spherical and fragmented material with an average size of 100-200 nm (Fig. 11).

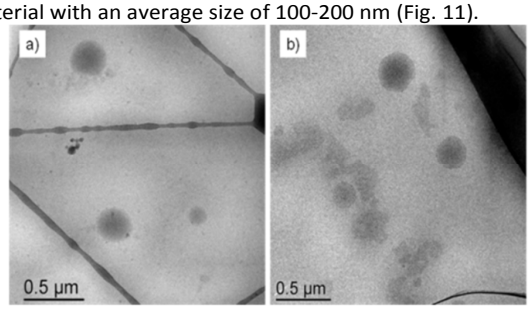

Fig. 11: a,b) Cryo-TEM pictures of 87/13 (v/v) water/methanol dispersions of **TPAP** at 4.5×10^{-5} M.

TPAP as environmental fluorescent probe in living cells

The last set of experiments established **TPAP** as environmental probe in living cell, on account of its sensitivity to local viscosity and polarity. At first, **TPAP** was added to the external medium of Hamster Ovary Cells (CHO) and its intracellular distribution was evaluated by confocal imaging. Within a few minutes from administration, **TPAP** was found to internalize effectively inside the cells, without affecting their viability. The dye mostly distributed in the endoplasmic reticulum (ER), and in internalization vesicles (Fig. 12). This partition into internal membrane organelles follows the moderate lipophilic nature of **TPAP**, and it is in agreement with the intracellular distribution of other neutral and lipophilic dyes.[37]

The ability of **TPAP** to evaluate local polarity and viscosity was assessed by two complementary techniques, which independently monitor the spectral and lifetime features of the probe, respectively. Both techniques are based on the "phasor analysis" approach developed by the Gratton's group.[42,43] In the phasor analysis, the spectral or lifetime profile of each pixel is Fourier-transformed to produce a vector (phasor) represented in a 2D plot named "phasor plot". Two cartesian (G and S) or polar (phase and modulation) coordinates pinpoint any phasor. In the *spectral* phasor plot, the angular coordinate (phase) is proportional to the spectral center of mass; the radial coordinate (modulation) is inversely related to the spectral width. A red-shift in wavelength leads to an increase of the angular position, whereas a decrease in spectral width increases the radius of the phasor. In the *lifetime* phasor plot, longer lifetimes are associated with larger phase and smaller modulation values. Notably, monoexponential lifetimes map out onto a semicircle of radius ½ and center (1/2,0).

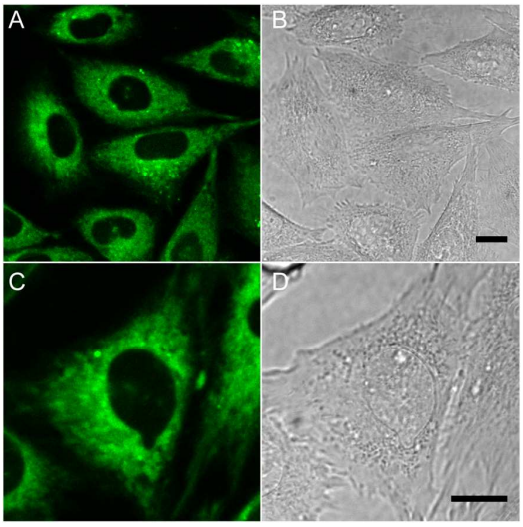

Fig. 12: A,C) Fluorescence confocal images revealing intracellular localization of **TPAP** in CHO cells and B,D) corresponding transmission images. Scale bar in B,D: 10 μm.

A cluster of points in any phasor plot corresponds to pixels with similar spectra or lifetimes. Phasor clusters in different positions identify different population/structures in target samples. Thus, the phasor approach provides an ideal tool for hyper-spectral and/or lifetime imaging analysis. Importantly, phasor combinations follow simple vectorial addition rules. For instance, the phasor of a two-component mixture inevitably falls on a line connecting the two phasors of the pure species. The distance from the resultant phasor to the individual "reference" phasors is inversely proportional to the contribution of that component, allowing for the calculation of the intensity fraction associated with each species. Several groups, including us, applied successfully the phasor analysis to follow a broad range of intracellular processes.[38,39]

The intracellular polarity analysis by **TPAP** was carried out by sequentially collecting 57 fluorescence confocal images from 430 to 600 nm on a target cell region. Fig. 13A shows the sum of all images and represents the whole emission in the 430–600 nm range. Fig. 13B displays the *spectral* phasor plot relevant to the spectral acquisition. We investigated the phasor clouds relevant to two different cell organelles, namely internalization vesicles (Fig. 13A, cyan arrow) and the ER (Fig. 13A, yellow arrow). The pixels relevant to the two organelles (Fig. 13C) mapped out different phasor regions, which were enclosed by coloured squares in Fig. 13B. Notably, these regions were unlike in term of phase angles (ER: -135° to -180°; vesicles: -225° to -300°), indicating large spectral differences between these two organelles. Indeed, vesicles were associated with a significant wavelength blue-shift (λ_{max} = 480 nm) as compared to ER (λ_{max} = 500 nm) (Figure 13D), although the Lippert-Mataga calibration of **TPAP** highlighted rather hydrophobic environments in both cases. These findings may suggest that **TPAP** sensed a lower polarity in vesicles than in the ER. Alternatively, the higher **TPAP** concentration in vesicles

(see intensity differences in Fig. 13A) led to significant dye aggregation and yielded blue-shift likewise what observed for **TPAP** nanoparticles (*vide supra*).

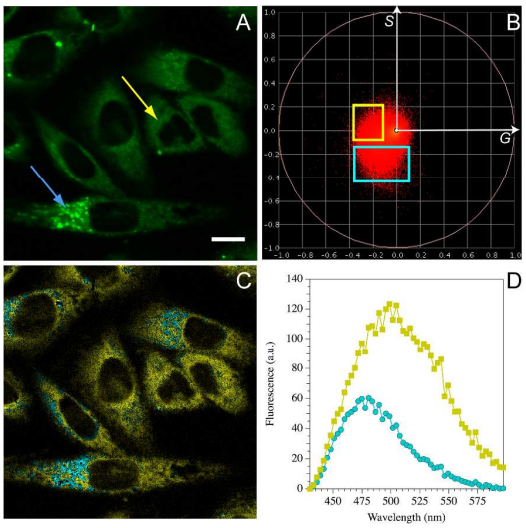

Fig. 13: Polarity analysis of living CHO cells by **TPAP** emission according to the phasor approach. A) Global fluorescence confocal image of CHO cells obtained scanning the emission interval from 430 to 600 nm in 59 steps; two representative cell vesicle and ER regions are indicated by a cyan and a yellow arrow, respectively; B) *Spectral* phasor of the 430–600 nm stack of images: two distinguishable phasor regions were enclosed in two colored squares; C) Phasor separation in the confocal image: the pixels corresponding to phasors in the cyan and yellow squares of panel B) are colored accordingly, highlighting cell vesicles and the ER; D) Spectra of phasor regions enclosed in the cyan and yellow squares: each spectrum has the same color code. Scale bar in A): 10 μm.

Next, we carried out intracellular viscosity measurements by inspecting the fluorescence lifetime of **TPAP**. Fig. 14A reports the collective *lifetime* phasor plot relevant to 19 cell fields. Notably, **TPAP** showed phasor clouds falling within the universal circle (Fig. 14A). This indicates that **TPAP** emission is no more monoexponential. Nonetheless, multiexponential decays are often encountered when rotors are embedded in complex cellular domains and reflect the environmental heterogeneity at nanoscale.[40,41] A second striking feature of the phasor clouds was their almost linear distribution. This arrangement prompted us to consider each **TPAP** phasor as an intensity-weighted sum of two reference phasors lying on the universal circle, on account of the vector additivity rule of phasors.[42] The reference phasors ***H*** and ***L*** were identified by the intersections between the universal circle and the linear fit of the global phasor cloud associated with all normal cells.

As a matter of fact, this approach correspond to a graphical deconvolution of the lifetime decay into two monoexponential components (τ_H = 4.37 ns, τ_L = 1.47 ns) for each pixel of any image.[43]

H and ***L*** identify two limit conditions of high and low local viscosities, respectively.[41] The map of intensity fraction relevant to ***H*** ($\mathbf{X}_H$) was calculated for each image by simple vector algebra.[44] Inspection of the ***H*** maps (Fig. 14D,G) provided a simple and straightforward way to compare relative viscosities of intracellular domains. **TPAP** entrapped in internalization vesicles (Fig. 14B white arrow sensed higher viscosity ($\langle \mathbf{X}_H \rangle$ = 0.827 ± 0.043) than in the ER (Fig. 14B, purple arrow; $\langle \mathbf{X}_H \rangle$ = 0.707 ± 0.036). Consistently, endosome vesicle membranes are about 3 times richer in cholesterol (the most relevant stiffening factor of biomembranes) than the ER.[45] Higher viscosity could be also brought about by dye aggregation in vesicles, inducing concomitantly a blue-shift of emission as discussed before.

Even more remarkable was the capability of **TPAP** to report the local viscosity of regions where its fluorescence is rather dim, namely chromatin in the cell nucleus (Fig. 14B,E, red arrow), and plasma membrane (Fig. 14E yellow arrow). In this context, the dividing cell of Figs. 14E-G nicely shows the fluidity of chromatin environment ($\langle \mathbf{X}_H \rangle$ = 0.598 ± 0.038) as compared with the rigid environment of plasma membrane ($\langle \mathbf{X}_H \rangle$ = 0.732 ± 0.068).

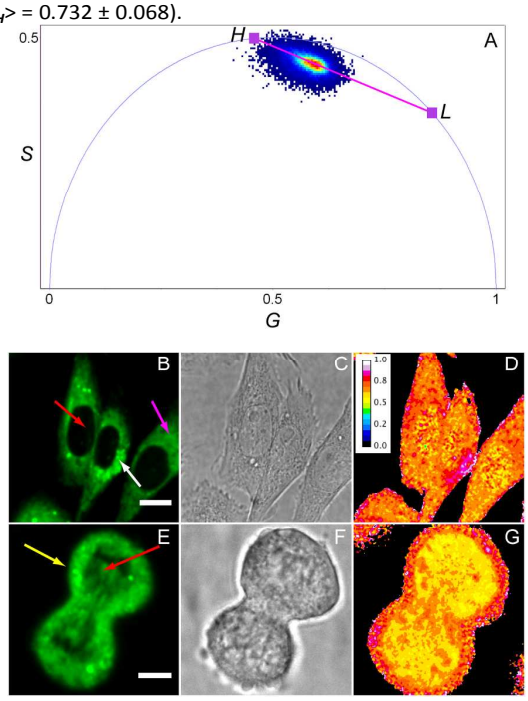

Fig. 14: Viscosity analysis of living CHO cells by **TPAP** lifetime according to the phasor approach. A) Collective *lifetime* phasor plot relevant to 19 cell images; the calibration line connecting the two reference phasors ***H*** and ***L*** is also reported; B,E) Fluorescence confocal images and corresponding C,F) transmission images and D,G) maps of ***H*** intensity fraction (X_H). Scale bars: B) 10 μm, E) 5 μm.

Conclusions

In summary, in this work we described the complete photophysical and computational characterization of **TPAP**, a new FMR. **TPAP** represents a derivative of highly-flexible molecular rotors, which exert barrier-less rotations independent of the solvent. Therefore, it belongs to the same

FMR family of **DPAP**, as its *modus operandi* lacks the presence of a TICT state. Instead, the emissive deactivation of the solvent-stabilized ICT state is either accompanied by triplet formation in non- and medium-polar solvents, or by direct non-radiative conversion into the ground state in polar and protic solvents. As compared to its parent analog (**DPAP)**, **TPAP** is 2-3 fold more emissive and it is associated with a solvatochromism that spans an interval of 150 nm, resulting in Stokes' shifts larger than 200 nm in high polar solvents. At the same time, a sensitive viscosity dependence of the **TPAP** emission was established. Hence, with the help of spectroscopic and microscopic techniques, information on the emissive and structural properties of **TPAP** nanoparticles has been also gathered. In particular, **TPAP** nanoparticles show a notable enhancement of emission intensity with lifetimes of up to 14 ns, as obtained from time-resolved studies, which is more than twice as long as lifetime of **TPAP** molecules in solution. On account of **TPAP** peculiar capability to report on local polarity and viscosity, we applied the probe to image confocally these features at intracellular level by a simple and straightforward graphic method named *phasor analysis*. Pleasantly, **TPAP** returned relative polarity and viscosity values of intracellular organelles (*e.g.*, endosomes, endoplasmic reticulum) that are in line with their compositions and structures. Further information on biological systems might be accessible by targeting specific subcellular regions via biofunctionalization of the rotor.

Acknowledgements

This work was supported by MIUR through FIRB (contract n° RBFR10DAK6 and RBFR12ETL5) and PRIN (contract n° 2012SK7ASN and 2010BJ23MN_004) projects. DREAMS Lab technical staff is kindly acknowledged for managing the computing facilities at SNS.

Notes and references

1. a) C, Reichardt, *Chem. Rev.*, 1994, **94**, 2319–2358. b) G. Signore, R. Nifosi, L. Albertazzi, B. Storti and R. Bizzarri, *J. Am. Chem. Soc.*, 2010, **132**, 1276–1288. c) G. S. Loving, M. Sainlos and B. Imperiali, *Trends Biotechnol.*, 2010, **2**, 73–83. d) X. Peng, Z. Yang, J. Wang, J. Fan, Y. He, F. Song, B. Wang, S. Sun, J. Qu, J. Qi and M. Yan, *J. Am. Chem. Soc.*, 2011, **133**, 6626–6635. e) A. Battisti, S. Panettieri, G. Abbandonato, E. Jacchetti, F. Cardarelli, G. Signore, F. Beltram and R. Bizzarri, *Anal. Bioanal. Chem.*, 2013, **405**, 6223–6233. f) G. Brancato, G. Signore, P. Neyroz, D. Polli, G. Cerullo, G. Abbandonato, L. Nucara, V. Barone, F. Beltram and R. Bizzarri, *J. Phys. Chem. B*, 2015, **119**, 6144–6154.
2. N. Mataga, Y. Kaifu and M. Koizumi, *Bull. Chem. Soc. Jpn.*, 1956, **29**, 465−470.
3. D. Marsh, *Biophys. J.*, 2009, **96**, 2549−2558.
4. A. K. Satpati, M. Kumbhakar, S. Nath and H. Pal, *Photochem. Photobiol.*, 2009, **85**, 119−129.
5. H. Weitman, M. Roslaniec, A. A. Frimer, M. Afri, D. Freeman, Y. Mazur and B. Ehrenberg, *Photochem. Photobiol.*, 2001, **73**, 110−118.
6. M. K. Kuimova, *Phys. Chem. Chem. Phys.*, 2012, **14**, 12671−12686
7. M. A. Haidekker and E. A. Theodorakis, *Org. Biomol. Chem.*, 2007, **5**, 1669−1678.
8. M. T. Stockl, R. Bizzarri and V. Subramaniam, in *Properties and Functions of Biological Membranes Investigated by Fluorescence Methods*, eds. Y. Mély and G. Duportail, Springer, Berlin Heidelberg, 2012, vol. 3, pp. 215−240.
9. T. Forster and G. Hoffmann, *Z. Phys. Chem.*, 1971, **75**, 63−76.
10. M. A. Haidekker and E. A. Theodorakis, *J. Biol. Eng.*, 2010, **4**, 11.
11. M. A. Haidekker, T. P. Brady, D. Lichlyter and E. A. Theodorakis, *Bioorg. Chem.*, 2005, **33**, 415−425.
12. M. A. H. Alamiry, A. C. Benniston, G. Copley, K. J. Elliott, A. Harriman, B. Stewart and Y. G. Zhi, *Chem. Mater.*, 2008, **20**, 4024−4032.
13. M. Koenig, G. Bottari, G. Brancato, V. Barone, D. M. Guldi and T. Torres, *Chem. Sci.*, 2013, **4**, 2502−2511.
14. a) J. Luo, Z. Xie, J. W. Y. Lam, L. Cheng, H. Chen, C. Qiu, H. S. Kwok, X. Zhan, Y. Liu, D. Zhu and B. Z. Tang, *Chem. Commun.*, 2001, 1740–1741. b) Y. Hong, J. W. Y. Lam and B. Z. Tang, *Chem. Soc. Rev.*, 2011, **40**, 5361–5388. c) Y. Hong, J. W. Y. Lam and B. Z. Tang, *Chem. Commun.*, 2009, 4332–4353. d) J. Mei, N. L. C. Leung, R. T. K. Kwok, J. W. Y. Lam and B. Z. Tang, *Chem. Rev.*, 2015, DOI: 10.1021/acs.chemrev.5b00263
15. A. Warshel and A. Dryga, *Proteins*, 2011, **79**, 3469−3484.
16. A. Warshel, P. K. Sharma, M. Kato and W. W. Parson, *Biochim. Biophys. Acta*, 2006, **1764**, 1647−1676.
17. D. A. Cherepanov, B. A. Feniouk, W. Junge and A. Y. Mulkidjanian, *Biophys. J.*, 2003, **85**, 1307−1316.
18. M. Stefl, N. G. James, J. A. Ross and D. M. Jameson, *Anal. Biochem.*, 2011, **410**, 62−69.
19. L. Giribabu, V. K. Singh, Ch. Vijay Kumar, Y. Soujanya, P. Yella Reddy and M. Lakshmi Kantam, *Sol. Energy*, 2011, **85,** 1204–1212.
20. Δf is reasonably suitable to describe the effects in non-protic solvents, where specific solvent solute interactions such as hydrogen bonding, etc. are absent. However, these specific solvent effects can be identified as deviations from the theory.
21. J. R. Lakowicz, *Principles of Fluorescence Spectroscopy*, Plenum Press, New York, 2006.
22. P. Minei, M. Koenig, A. Battisti, M. Ahmad, V. Barone, T. Torres, D. M. Guldi, G. Brancato, G. Bottari and A. Pucci, *J. Mater. Chem. C*, 2014, **2**, 9224-9232.
23. A. Hakonen, J. E. Beves and N. Stromberg, *Analyst*, 2014, **139**, 3524-3527.
24. Singlet oxygen quantum yields are used as a measure for triplet excited state generation.
25. A. A. Abdel-Shafi and F. Wilkinson, *Phys. Chem. Chem. Phys.*, 2002, **4**, 248–254.
26 L. Reynolds, J. A. Gardecki, S. J. V. Frankland, M. L. Horng and M. Maroncelli, *J. Phys. Chem.*, 1996, **100**, 10337−10354.
27. a) K. Y. Law, *Chem. Phys. Lett.*, 1980, **75**, 545–549. b) R. O. Loutfy and B. A. Arnold, *J. Phys. Chem.*, 1982, **86**, 4205–4211.
28. T. Foerster and G. Z. Hoffmann, *Phys. Chem.*, 1971, **75**, 63–76.
29. J. Sutharsan, D. Lichlyter, N. E. Wright, M. Dakanali, M. A. Haidekker and E. A. Theodorakis, *Tetrahedron*, 2010, **66**, 2582-2588.
30. H. Nakanishi and H. Oikawa, *Reprecipitation method for organic nanocrystals*, In *Single Organic Nanoparticles* ed. H. Masuhara, H. Nakanishi and K. Sasaki, Springer-Verlag, Berlin, 2003, pp. 17–31.

31. M. Koenig, T. Torres, V. Barone, G. Brancato, D. M. Guldi and G. Bottari, *Chem. Commun.*, 2014, **50**, 12955−12958.
32. Considering the ICT nature of **TPAP** emission, we ascribe this effect to the decrease of non-radiative charge recombination processes upon lowering the temperature.
33. a) C. M. Heller, I. H. Campbell, B. K. Laurich, D. L. Smith, D. D. C. Bradley, P. L. Burn, J. P. Ferraris and K. Mullen, *Phys. Rev. B*, 1996, **54**, 5516−5522; b) Y. V. Ryabchikov, S. A. Alekseev, V. V. Lysenko, G. Bremond and J. M. Bluet, *Nanoscale Res. Lett.*, 2012, **7**, 365−369.
34. Such a dual emission has been previously observed in molecular aggregates of aromatic fluorophores and it has been attributed to emission from monomeric, localized and delocalized excited states.
35. a) K. Inoue and M. Itoh, *Bull. Chem. Soc. Jpn.*, 1979, **1**, 45−48. b) P. P. Neelakandan and D. Ramaiah, *Angew. Chem. Int. Ed.*, **2008**, *47*, 8407−8411.
36. Unless otherwise stated, 87/13 (v/v) is the optimal solvent ratio used for the preparation of the water/methanol **TPAP** dispersions.
37. G. Signore, G. Abbandonato, B. Storti, M. Stockl, V. Subramaniam and R. Bizzarri, *Chem. Commun.*, 2013, **49**, 1723−1725.
38. E. Hinde, M. A. Digman, K. M. Hahn and E. Gratton, *Proc. Natl. Acad. Sci. U S A*, 2013, **110**, 135−140.
39. A. Battisti, M. A. Digman, E. Gratton, B. Storti, F. Beltram and R. Bizzarri, *Chem. Commun.*, 2012, **48**, 5127−5129.
40. Y. L. Wu, M. Stefl, A. Olzynska, M. Hof, G. Yahioglu, P. Yip, D. R. Casey, O. Ces, J. Humpolickova and M. K. Kuimova, *Phys. Chem. Chem. Phys.*, 2013, **15**, 14986−14993.
41. G. Ferri, L. Nucara, T. Biver, A. Battisti, G. Signore and R. Bizzarri, *Biophys. Chem.*, 2016, **208**, 17-25.
42. D. M. Jameson, E. Gratton and R. D. Hall, *Appl. Spectrosc. Rev.*, 1984, **20**, 55−106.
43. M. A. Digman, V. R. Caiolfa, M. Zamai and E. Gratton, *Biophys. J.*, 2008, **94**, L14−16.
44. K. M. Hirshfield, D. Toptygin, B. S. Packard and L. Brand, *Anal. Biochem.*, 1993, **209**, 209−218.
45. G. van Meer, D. R. Voelker and G. W. Feigenson, *Nat. Rev. Mol. Cell Biol.*, 2008, **9**, 112−124.

Supporting Information for

"A fluorescent molecular rotor showing vapochromism, aggregation-induced emission, and environmental sensing in living cells"

Matthias Koenig,[d] Barbara Storti,[e] Ranieri Bizzarri,[e] Dirk M. Guldi,[d] Giuseppe Brancato*[c] and Giovanni Bottari*[ab]

[a] Departamento de Química Orgánica, Universidad Autónoma de Madrid, 28049, Cantoblanco, Spain

[b] IMDEA-Nanociencia, Campus de Cantoblanco, C/Faraday 9, 28049 Madrid, Spain

[c] Scuola Normale Superiore, Piazza dei Cavalieri 7, I-56126 Pisa, Italy

[d] Department of Chemistry and Pharmacy & Interdisciplinary Center for Molecular Materials (ICMM), Friedrich-Alexander-Universität Erlangen-Nürnberg, 91058, Erlangen, Germany

[e] Materials (ICMM), Friedrich-Alexander-Universität Erlangen-Nürnberg, 91058, Erlangen, Germany

Abbreviations

Cryo−TEM = cryogenic − transmission electron microscopy; DFT = density functional theory; DLS = dynamic light scattering; DMSO = dimethylsulfoxide; **DPAP** = 4-(diphenylamino)-phthalonitrile; n = refractive index of a solvent; NMR = nuclear magnetic resonance; PCM = Polarizable Continuum Model; k_R = radiative decay constant; k_{NR} = non-radiative decay constant; QM = quantum mechanical; TD−DFT = time-dependent density functional theory; TLC = thin layer chromatography; **TPAP** = 4-(triphenylamino)-phthalonitrile; Δf = Lippert-Mataga solvent parameter; ε = dielectric constant; Φ_{fl} = fluorescent quantum yield; τ_R = emission lifetime.

Materials and Methods

Chemicals and solvents were purchased from Aldrich and used without further purification. NMR spectra (^{1}H and ^{13}C) were recorded with a Bruker Advance 300 MHz instrument. IR spectra were recorded on a Bruker Vector 22 spectrophotometer employing in all cases solid samples (KBr pressed disks). EI-MS spectra were obtained from a VG AutoSpec spectrometer. Column chromatography was carried out on silica gel Merck-60 (230-400 mesh, 60Å). Analytical TLC was performed on aluminium sheets precoated with silica gel 60 F-254 from Merck.

Photophysical studies

All solvents were spectroscopic grade and were purchased from various commercial suppliers (Sigma-Aldrich, Merck and Roth). Dielectric constants, refractive indices, and viscosities of the pure solvents were obtained from the literature.[1] UV/vis spectra were recorded with a Perkin Elmer Lambda 2 instrument and steady-state emission with a FluoroMax 3 fluorometer by HORIBA JobinYvon using a quartz cell with 10 mm optical path length. For emission below room temperature, a Haake KT40 thermostat/cryostat was installed, while for emission above room temperature samples were heated using a Haake NB22 thermostat. Fluorescence lifetimes and time-resolved emission were measured with a HORIBA JobinYvon Fluorolog instrument. For excitation, a NanoLED 295 nm and 403 nm light source was used. This instrument was also used to detect emission in the NIR-region. Femtosecond transient absorption studies were performed in argon-saturated solutions with 387 nm excitation laser pulses (1 kHz, 150 fs pulse width) from an amplified Ti:Sapphire laser system (Clark-MXR Inc.) with a laser energy of 200 nJ. Nanosecond laser flash photolysis experiments were carried out with argon or oxygen purged samples using a 355 nm laser pulse from a Quanta-Ray CDR Nd:Yag system (6 ns pulse width) in a front face excitation geometry.

Cryo−TEM studies

For Cryo−TEM studies, a drop of the dispersion (87/13 methanol/water mixture) was put on a lacey carbon-coated copper TEM grid (200 mesh, Science Services) where most of the liquid was removed with blotting paper, leaving a thin film stretched over the grid holes. The specimens were instantly shock vitrified by rapid immersion into liquid ethane and cooled to approximately 90 K by liquid nitrogen in a temperature-controlled freezing unit (Zeiss Cryobox, Zeiss SMT GmbH). The temperature was monitored and kept constant in the chamber during all the sample preparation steps. After the sample is frozen, it was inserted into a cryo-transfer holder (CT3500, Gatan) and transferred to a Zeiss EM922 Omega EF-TEM. Examinations were carried out at temperatures around 90 K at an acceleration voltage of 200 kV. Zero-loss filtered images (ΔE = 0 eV) were taken under reduced dose conditions (100–1000 electrons/nm^2). All images were registered digitally by a bottom-mounted CCD camera system (Ultrascan 1000, Gatan) combined and processed with a digital imaging processing system (Gatan Digital Micrograph 3.9 for GMS 1.82).

DLS studies

DLS data were collected with a Zetasizer Nano ZS in back scatter mode with a He-Ne laser (λ_{exc} = 633 nm) using quartz cells with 10 mm optical path length at 25°C. All measurements were preceded by 1 min. equilibration time and for each probe, 5 measurements consisting of 5 runs each were applied. The DLS measurements imply spherical particles.

Computational details

Quantum mechanical (QM) calculations of the structural and optical properties of **TPAP** have been carried out by methods rooted into density functional theory (DFT) and its time-dependent extension (TD-DFT).[2] Here, a hybrid functional (B3LYP)[3] and its long-range corrected extensions (CAM-B3LYP)[4] has been used, since it was found appropriate for describing molecular systems with an extended electronic delocalization. The 6-31G*(d,p) basis set has been used in all calculations. Solvent effects have been included by means of the conductor-like version of the Polarizable Continuum Model (C-PCM).[5] In particular, an apolar (*i.e.*, hexane) and a polar (*i.e.*, acetonitrile) solvent were considered to investigate polarity effects. Vertical transition energies have been computed within the usual linear response approximation in case of optical absorption, whereas a state-specific PCM calculation has been carried out for optical emission calculations.[6] In the latter case, molecular structures corresponding to the first singlet excited state have been relaxed before emission calculations using analytical gradients.[7] Optical spectra have been evaluated from a convolution of excitation (or emission) calculations on molecular structures generated from a scan about the relevant torsional angle (see Fig. S1). To this end, the 1,2-dicyanobenzene moiety was rotated in step of 10° and the computed excitation (emission) transitions were weighted according to a Boltzmann distribution and, then, Gaussian convoluted (σ = 2000 cm^{-1}). All quantum mechanical calculations have been carried out with the Gaussian09 software package.[8]

Fluorescence microscopy imaging of living cells

Living CHO, placed in glass bottom WillCo dishes, were treated for 15 min with 0.35 ml in 1 ml of a 5.4 mM of **TPAP** solution in DMSO, and then mounted in a thermostated chamber at 37 °C (Leica Microsystems) humidified with 5% CO_2 atmosphere.

Fluorescence imaging was carried out by a confocal scanning laser microscope Leica TCS SP5 (Leica Microsystems, Mannheim, Germany) according to two operating modes: confocal

imaging and confocal FLIM. For confocal imaging, cells were observed by exciting at 405 nm with a pulsed diode laser operating at 40 MHz (average power: 10–20 mW at the sample) and collecting the emission in the 500-580 nm range. Spectral images were collected by acquiring sequentially cell fluorescence in 5-nm emission intervals from 430 to 600 nm. For confocal FLIM, cells were observed by collecting the emission in the 500-580 nm range by a photomultiplier tube interfaced with a Time Correlated Single Photon Counting card and setup (PicoHarp 300, PicoQuant, Berlin); FLIM acquisitions lasted until 100-200 photons were collected on average in each pixel.

In all imaging modes, cells were viewed with a 40 × 1.25 NA or 100 × 1.4 NA oil immersion objectives (Leica Microsystems, Berlin, Germany). Line scanning speeds ranged from 200 to 1400 Hz, depending on the sample fluorescence and optical zoom. The pinhole aperture was set to 1.0 Airy. Imaging data were analyzed by ImageJ software (National Institutes of Health, Bethesda, MD).

For *spectral* phasor analysis, spectral image stacks were elaborated using the Space-Time plugin of ImageJ (available at www.spechron.com/Spectral%20Phasor-Download.aspx).

For *lifetime* phasor analysis, confocal FLIM images were elaborated using SimFCS software (available at www.lfd.uci.edu).

Synthesis of 4-(triphenylamino)-phthalonitrile (TPAP)

TPAP was prepared and purified following a reported procedure.[9] Yield: 88%. ^{1}H NMR (300 MHz, $CDCl_3$) δ (ppm) 8.40 (d, 1H, J = 4.8 Hz); 8.25 (dd, 2H, J = 6.8 Hz); 7.95 (s, 1H); 7.80 (m, 4H), 7.30 (m, 3H), 7.10 (m, 6H); IR (KBr): 3058, 2925, 2855, 2226, 1729, 1583, 1487, 1071, 813; ESI-MS (m/z): $C_{26}H_{17}N_3$ [371.4]: $[M]^+$ 371.4. Elemental analysis for $C_{26}H_{17}N_3$: Calculated: C, 84.07; H, 4.61; N, 11.31; Found C, 84.18; H, 4.68; N, 11.21.

Table S1. This table resumes some physical properties of the solvents, solvent mixtures and PMMA matrix used in this study such as the dielectric constant (ε), the refractive index of the solvent (n) and the Lippert-Mataga solvent parameter (Δf)[10] as well as the fluorescent quantum yield (Φ_{fl}), emission lifetime (τ_R), radiative (k_R) and non-radiative (k_{NR}) decay constant for **TPAP** in the listed solvents. The solvents in the table are organized from the lower (top) to the higher (bottom) Δf values.

Solvent	n	ε	Δf	Φ_{fl}	τ_{fl} (ns)	k_R (ns^{-1})	k_{NR} (ns^{-1})
cyclohexane	1.426	2.023	0	1	2.82	0.3546	0
o-xylene	1.496	2.568	0.0295	0.86	3.55	0.2423	0.0394
anisole	1.518	4.33	0.1122	0.75	4.4	0.1705	0.0568
tetrahydrofurane	1.407	7.52	0.2089	0.47	5.44	0.0864	0.0974
anisole/benzonitrile (6/4)	1.523	12.7	0.2091	0.41	5.67	0.0723	0.1041
dichloromethane	1.424	8.93	0.2172	0.42	6.21	0.0676	0.0934
anisole/benzonitrile (4/6)	1.525	16.9	0.2222	0.37	5.55	0.0667	0.1135
benzonitrile	1.53	25.2	0.2348	0.33	4.68	0.0705	0.1432
n-hexanol	1.418	13.3	0.2430	0.202	3.1	0.0652	0.2574
methyl isopropyl ketone	1.39	12.4	0.2502	0.197	4.55	0.0433	0.1765
dimethylsulfoxide	1.477	48	0.2642	0.034	0.94	0.0362	1.0277
dimethylformamide	1.43	37	0.2754	0.048	1.45	0.0331	0.6566
ethylene glycol	1.432	41.4	0.2761	0.0061	0.14	0.0424	6.9021
acetonitrile	1.344	37.5	0.3055	0.04	1.34	0.0299	0.7164
methanol	1.326	33.8	0.3102	0.0026	0.17	0.0151	5.7988

$$\Delta f = \frac{\varepsilon - 1}{2\varepsilon + 1} - \frac{n^2 - 1}{2n^2 + 1} \quad \text{(eq. S1a)}$$

$$\varepsilon_{MS} = f_A \varepsilon_A + f_B \varepsilon_B$$

$$n_{MS}{}^2 = f_A n_A{}^2 + f_B n_B{}^2 \quad \text{(eq. S1b,c)}$$

In eq. S1a, which allows to calculate the Lippert-Mataga solvent parameter Δf, ε is the dielectric constant and n is the refractive index of the solvent. Eq. 1b,c were used to calculate the dielectric constant and refractive index of the solvent mixtures.

$$k_R = \Phi_{fl}/\tau_R \quad \text{(eq. S2a)}$$

$$k_{NR} = (1 - \Phi_{fl})/\tau_R \quad \text{(eq. S2b)}$$

Eq. S2a allows to calculate the radiative decay rate constants. Eq. 2b was used to calculate the non-radiative decay rate constants.

Table S2. Lippert-Mataga polarity parameter (Δf) and non-radiative decay constants k_1 and k_2 as determined from transient absorption spectroscopy for **TPAP** in solvents with variable polarities and viscosities (at 293-298 K)

Solvent	Δf	η (cP)	k_1 (ns^{-1})	k_2 (ns^{-1})
o-xylene	0.0295	0.81	10.0	0.23
tetrahydrofuran	0.2089	0.48	11.8	0.17
acetonitrile	0.3055	0.34	31	0.88
methanol	0.3102	0.52	90	5.19
ethylene glycol	-	16.9	28	3.6
ethylene glycol/glycerol (1:1)	*nd*	115	15	3.0
glycerol	-	1179	9.4	1.4

Table S3: Emission lifetimes and amplitudes for **TPAP** (4.5×10^{-5} M) in methanol and in 87/13 (v/v) methanol/water dispersions.

	τ_1 (ns)	τ_2 (ns)	A1 (%)	A2 (%)
methanol **TPAP** solution	0.17	–	–	–
TPAP dispersion	12.9	3.9	55	45
frozen **TPAP** dispersion	14.3	4.4	50	50

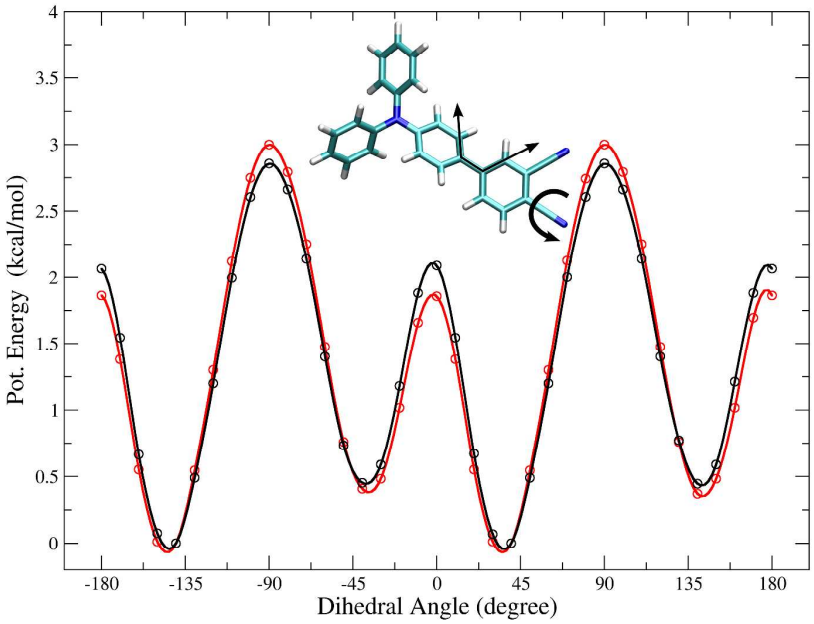

Figure S1: Computed torsional potential of the 1,2-dicyanobenzene moiety with respect to the rest of the molecule in hexane (black) and acetonitrile (red). The considered dihedral angle and rotational motion are depicted along with the molecular structure. QM calculations were performed according to the B3LYP/6-31G*(d,p) level of theory, including solvent effects implicitly.

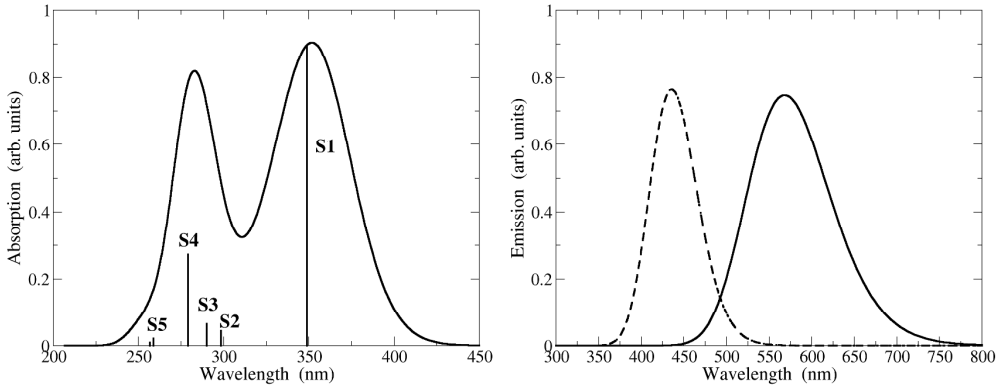

Figure S2: Computed optical absorption (left panel) and emission (right panel) spectra of **TPAP** in solution. Excitation transition energies and intensities are also shown as a stick spectrum in absorption. Solid line, acetonitrile; dashed line, hexane.

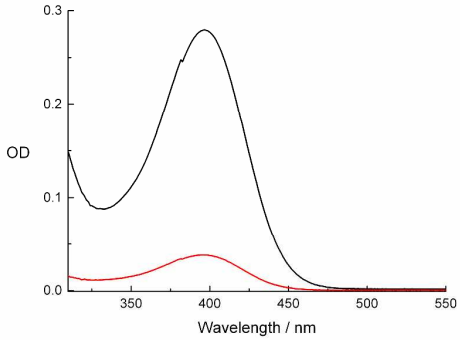

Figure S3: Absorption spectra of **TPAP** (2.5×10^{-6} M) in pyridine (black) and dichloromethane (red).

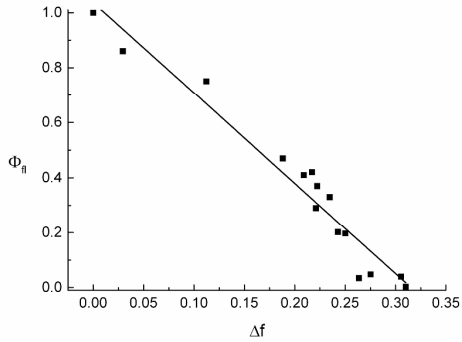

Figure S4: Plot of the Lippert-Mataga solvent parameter (Δf) *vs* the fluorescence quantum yield (Φ_{fl}) of **TPAP** in various solvents.

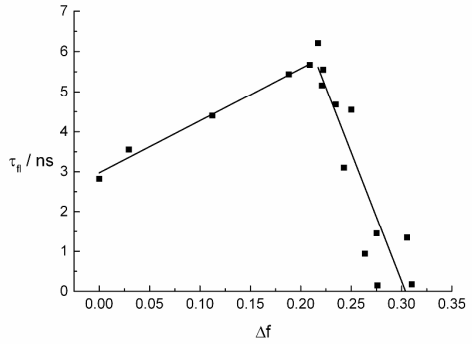

Figure S5: Plot of the fluorescence lifetimes (τ_{fl}) of **TPAP** as a function of the solvent parameter Δf.

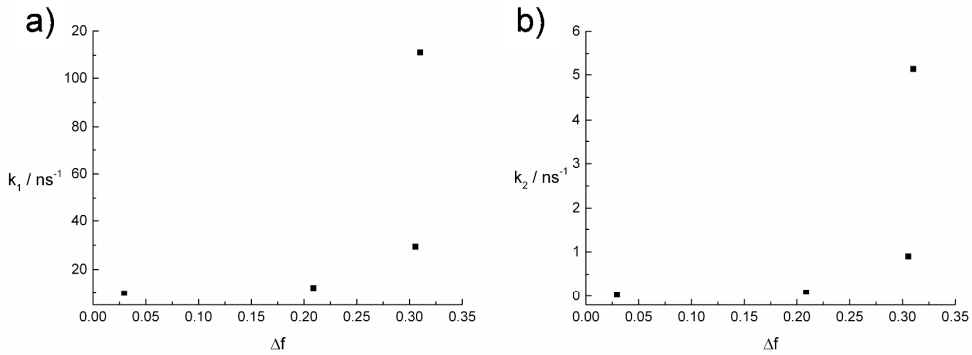

Figure S6: Plot of the Lippert-Mataga solvent parameter (Δf) *vs* a) the decay rate constant k_1 and b) the decay rate constant k_2 for **TPAP** in argon-saturated *o*-xylene, THF, acetonitrile and methanol obtained upon femtosecond flash photolysis.

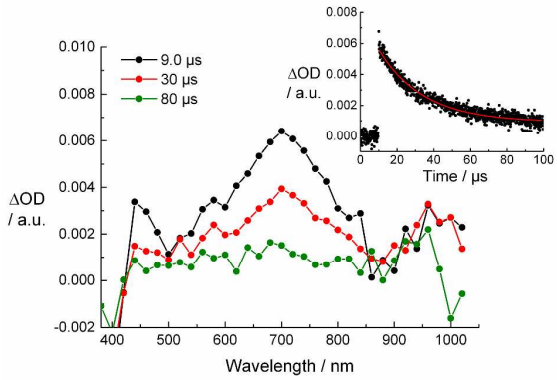

Figure S7: Differential absorption spectra obtained upon nanosecond flash photolysis of **TPAP** in argon-saturated THF with different time delays. OD at the 355 nm excitation wavelength was 0.2. Inset: Corresponding time-absorption profile at 720 nm.

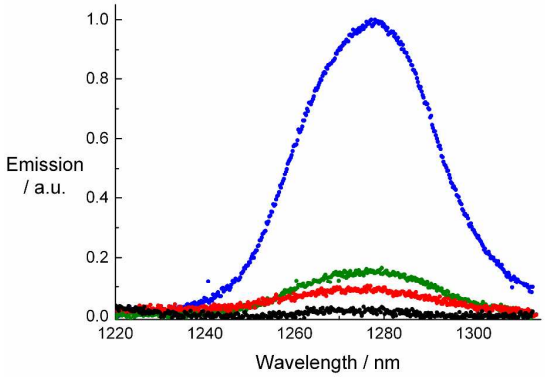

Figure S8: Singlet oxygen phosphorescence spectra of **TPAP** in *o*-xylene (green), THF (red), and acetonitrile (black) as well as the reference free-base tetraphenylporphyrin (blue) measured at room temperature in oxygen saturated solutions. OD at the excitation wavelength (403 nm) was 0.1 for all samples.

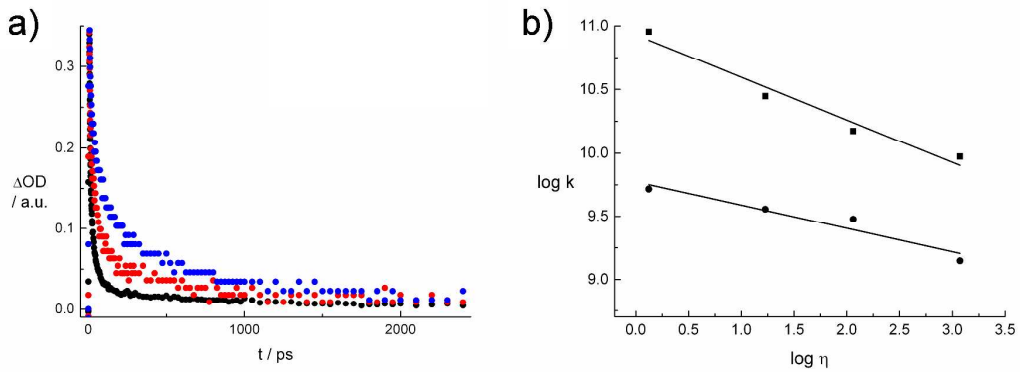

Figure S9: (a) Time–absorption profiles in ethylene glycol (black), ethylene glycol/glycerine (1:1; v/v) (red) and glycerine (blue) at around 900 nm obtained from femtosecond flash photolysis experiments (λ_{exc} = 387 nm). (b) Double-logarithmic plot of the solvent viscosity (η) *vs* the non-radiative decay constants k_1 (squares) and k_2 (circles) as determined from transient absorption spectroscopy for **TPAP** based on the Förster-Hoffmann equation.

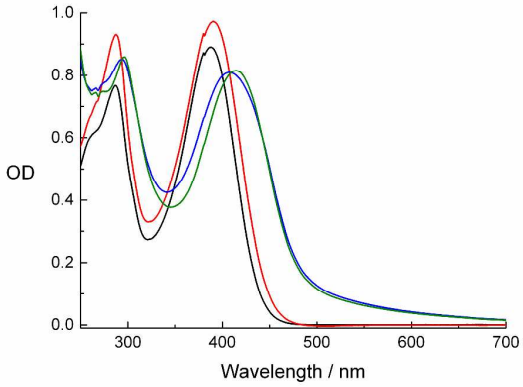

Figure S10: Absorption spectra of **TPAP** (4.5×10^{-5} M) in methanol (black) and in different water/methanol mixtures (45/55 (v/v) (red), 55/34 (v/v) (blue) and 87/13 (v/v) (green)).

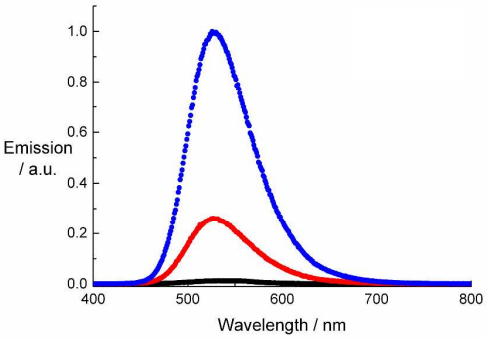

Figure S11: Emission spectra (λ_{exc} = 390 nm) of **TPAP** dispersions (87/13 (v/v) water/methanol mixture) at different concentrations, 1.1×10^{-6} M (black), 2.3×10^{-6} M (red) and 6.8×10^{-6} M (blue).

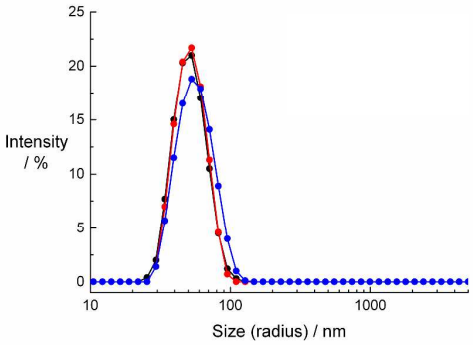

Figure S12: DLS of **TPAP** dispersions at different concentrations ([**TPAP**] = 2.25×10^{-5} M (black), 4.5×10^{-5} M (red), 5.0×10^{-4} M (blue)) in a 87/13 (v/v) water/methanol mixture.

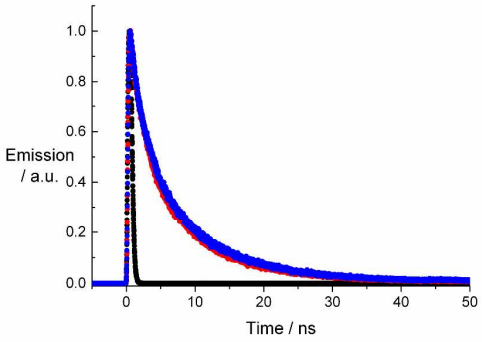

Figure S13: Time fluorescence profiles of **TPAP** (4.5×10^{-5} M) in methanol (black) and in an 87/13 (v/v) water/methanol mixture at room temperature (red) and frozen (blue).

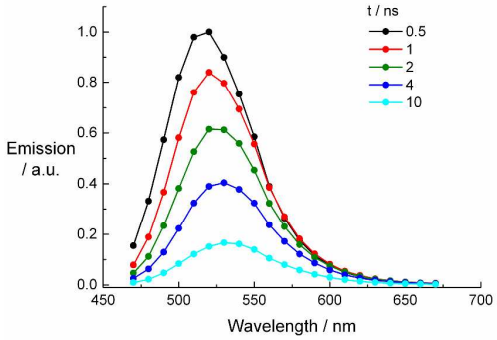

Figure S14: Time-resolved fluorescence spectra of a dispersion of **TPAP** ([**TPAP**] = 4.5×10^{-5} M, 87/13 (v/v) water/methanol mixture) after different time delays.

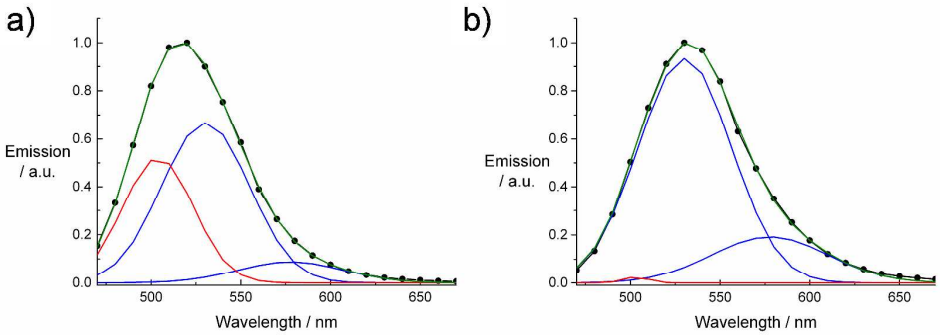

Figure S15: Deconvolution of the time-resolved fluorescence spectra of a dispersion of **TPAP** ([**TPAP**] = 4.5×10^{-5} M, 87/13 (v/v) water/methanol mixture) (black) after a) 0.5 ns and b) 10 ns. The Gauss functions (blue and red) and a sum fit (green) are included.

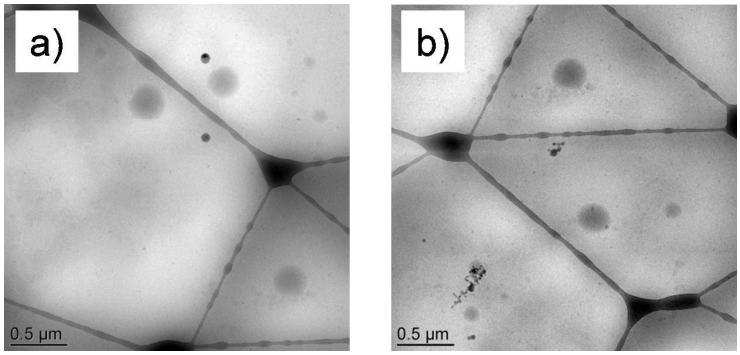

Figure S16: a,b) Cryo-TEM pictures of 87/13 (v/v) water/methanol dispersions of TPAP at 4.5×10^{-5} M.

Supporting references section

1. a) H. G. O. Becker, *Einführung in die Photochemie*, Georg Thieme Verlag, Stuttgart, 1983. b) I. M. Smallwood, *Handbook of Organic Solvent Properties*, Elsevier, 1996. c) M. Holdefer, *Relative Dielektrizitätskonstante εr (DK-Werte) von flüssigen und festen Medien*, Endress+Hauser Messtechnik GmBH+Co., Weil am Rhein, 1999. d) N. P. Cheremisinoff, *Industrial Solvents Handbook*, 2nd edition, Princeton Energies Resources International, Rockville, Maryland, U.S.A., 2003. e) N. S. Cheng, *Ind. Eng. Chem. Res.*, 2008, **47**, 3285–3288.
2. a) E. Runge and E. K. U. Gross, *Phys. Rev. Lett.,* 1984, **52**, 997–1000. b) M. E. Casida, Time-Dependent Density-Functional Response Theory for Molecules, in *Recent Advances in Density Functional Methods Volume 1*, ed. D. P. Chong, World Scientific, Singapore, 1995, pp 155–192.
3. a) A. D. Becke, *J. Chem. Phys.*, 1993, **98**, 5648–5652. b) P. J. Stephens, F. J. Devlin, C. F. Chabalowski and M. J. Frisch, *J. Chem. Phys.*, 1994, **98**, 11623–11627.
4. T. Yanai, D. P. Tew and N. C. A. Handy, *Chem. Phys. Lett.*, 2004, **393**, 51–57.
5. a) A. Klamt and G. Schüürmann, *J. Chem. Soc., Perkin Trans. 2*, 1993*,* 799–805. (b) V. Barone and M. Cossi, *J. Chem. Phys. A*, 1998, **102**, 1995–2001. (c) M. Cossi, N. Rega, G. Scalmani and V. Barone, *J. Comput. Chem.*, 2003, **24**, 669–681.
6. R. Improta, V. Barone, G. Scalmani and M. J. Frisch, *J. Chem. Phys.*, 2006, **125**, 054103.
7. G. Scalmani, M. Frisch, B. Mennucci, J. Tomasi, R. Cammi and V. Barone, *J. Chem. Phys*., 2006, **124**, 094107.

8. M. J. Frisch, G. W. Trucks, H. B. Schlegel, G. E. Scuseria, M. A. Robb, J. R. Cheeseman, G. Scalmani, et al. "Gaussian 09, Revision B.01," 2009.
9. L. Giribabu, V. K. Singh, Ch. Vijay Kumar, Y. Soujanya, P. Yella Reddy and M. Lakshmi Kantam, *Sol. Energy*, 2011, **85**, 1204–1212.
10. a) E. Z. Lippert, *Naturforsch.* **1955**, *10a*, 541. b) N. Mataga, Y. Kaifu, M. Koizumi, Bull. Chem. Soc. Jpn., 1956, **29,** 465−470. c) J. R. Lakowicz, *Principles of Fluorescence Spectroscopy*; Plenum Press: New York, 2006.

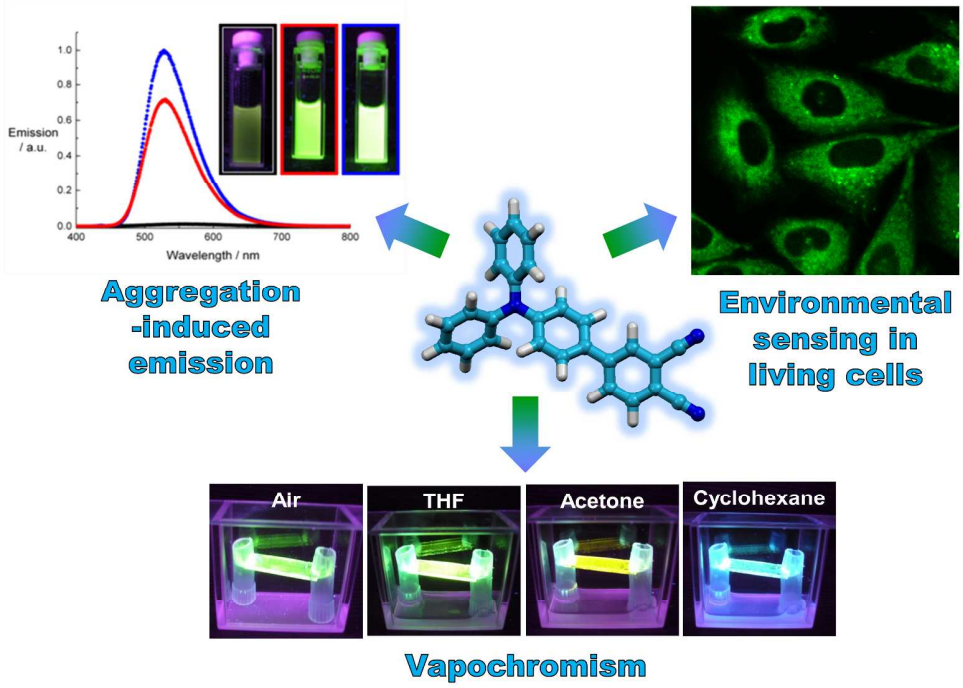

254x190mm (300 x 300 DPI)